Article

Tendencies in ABO$_3$ Perovskite and SrF$_2$, BaF$_2$ and CaF$_2$ Bulk and Surface *F*-Center Ab Initio Computations at High Symmetry Cubic Structure

Roberts I. Eglitis [1,*], **Juris Purans** [1], **Anatoli I. Popov** [1] **and Ran Jia** [1,2]

[1] Institute of Solid State Physics, University of Latvia, 8 Kengaraga Str., LV1063 Riga, Latvia; purans@cfi.lu.lv (J.P.); popov@ill.fr (A.I.P.); jiaran@jlu.edu.cn (R.J.)

[2] Laboratory of Theoretical and Computational Chemistry, Institute of Theoretical Chemistry, Jilin University, Changchun 130023, China

[*] Correspondence: rieglitis@cfi.lu.lv; Tel.: +371-26-426-703

Abstract: We computed the atomic shift sizes of the closest adjacent atoms adjoining the (001) surface *F*-center at ABO$_3$ perovskites. They are significantly larger than the atomic shift sizes of the closest adjacent atoms adjoining the bulk *F*-center. In the ABO$_3$ perovskite matrixes, the electron charge is significantly stronger confined in the interior of the bulk oxygen vacancy than in the interior of the (001) surface oxygen vacancy. The formation energy of the oxygen vacancy on the (001) surface is smaller than in the bulk. This microscopic energy distinction stimulates the oxygen vacancy segregation from the perovskite bulk to their (001) surfaces. The (001) surface *F*-center created defect level is nearer to the (001) surface conduction band (CB) bottom as the bulk *F*-center created defect level. On the contrary, the SrF$_2$, BaF$_2$ and CaF$_2$ bulk and surface *F*-center charge is almost perfectly confined to the interior of the fluorine vacancy. The shift sizes of atoms adjoining the bulk and surface *F*-centers in SrF$_2$, CaF$_2$ and BaF$_2$ matrixes are microscopic as compared to the case of ABO$_3$ perovskites.

Keywords: ab initio computations; B3PW; B3LYP; *F*-center; ABO$_3$ high symmetry cubic perovskites

1. Introduction

In the last 50 years, great attention has been paid to an in-depth understanding of the radiation formation of lattice defects in alkali and alkaline earth metal halides, as well as in simple and complex oxides. Several review articles were published, where both the mechanisms of their creation and the properties of the main defects were described in detail [1–5]. Lattice-point defects in these materials are traditionally called color centers and are classified into several large groups, among which electron centers, hole centers and interstitial particles are the most noticeable primary point radiation defects. As for electronic centers, *F*-centers are among the most intensively studied point defects in alkali and alkaline–halides. An ordinary *F*-center consists of one electron captured by a halogen vacancy [1,2,5]. Such *F* (*Farbe*) centers in alkali halides and alkaline–earth halides and oxides have been studied for many decades [1,2,5–12]. Thus, *F*-centers are defects in ionic crystals in which an anion is replaced by one or more trapped electrons. These vacancy-trapped electrons, confined and screened by the surrounding crystal lattice, thus form gap states with unique optical, electrical and magnetic properties [7–16] that are relevant to different optoelectronic devices. How efficient the formation is of point defects, including *F*-centers, is also the determining factor of the material radiation resistance in nuclear applications [17–21]. *F*-centers at surfaces, along with other anionic defects, are also relevant in catalysis [22].

The *F*-center in ABO$_3$ perovskites is the oxygen vacancy (V_0), which catches 2 electrons. The V_0 is the most frequent point defect in ABO$_3$ perovskites [23–27]. Bearing in mind the

technological relevance of ABO_3 perovskite matrixes, as well as quantity of *F*-centers, which unavoidably exist in these materials and deteriorate their quality, the number of *F*-center studies is still insufficient [28–35]. In order to save the computer time, we performed bulk and (001) surface *F*-center ab initio computations in ABO_3 perovskites in their high-symmetry cubic phase. The $SrZrO_3$, $PbTiO_3$, $BaTiO_3$ and $SrTiO_3$ cubic unit cells accommodate five atoms. The coordinates (0, 0, 0) have the A atom (A = Sr, Pb, Ba or Sr). It is placed at the corner position of the cube. The Ti atom is placed in the body center position of the cube, with the following coordinates ($\frac{1}{2}$, $\frac{1}{2}$, $\frac{1}{2}$). Finally, the three O atoms are placed in the face centered positions of the cube with the coordinates ($\frac{1}{2}$, $\frac{1}{2}$, 0), ($\frac{1}{2}$, 0, $\frac{1}{2}$) and (0, $\frac{1}{2}$, $\frac{1}{2}$). All our computed $SrZrO_3$, $PbTiO_3$, $BaTiO_3$ and $SrTiO_3$ perovskites at their high symmetry cubic structure belong to the space group $Pm3m$ with the space group number 221. Our computed $SrZrO_3$, $PbTiO_3$, $BaTiO_3$ and $SrTiO_3$ perovskites exhibit a large variety of different structural phase transitions from the high temperature and symmetry cubic paraelectric phase as the temperature is reduced. For example, the $SrZrO_3$ exhibits a cubic perovskite-type structure. The space group ($Pm3m$: 221) incorporates 48 symmetry operations. The Wyckoff positions for the atoms are as follows: Sr 1a (0.0, 0.0, 0.0), Zr 1b (0.5, 0.5, 0.5) and O 3c (0.0, 0.5, 0.5). The $SrZrO_3$ perovskite undergoes three phase transitions: orthorhombic (*Pnma*), orthorhombic with another space group (*Cmcm*), tetragonal (*I4/mcm*) and cubic (*Pm3m*) at temperatures of approximately 970, 1100 and 1440 K, respectively. In contrast, the $SrTiO_3$ crystal has a polar soft mode, but it does not exhibit a ferroelectric phase transition and always remains in its high symmetry cubic phase. Finally, $BaTiO_3$ is a perovskite that undergoes a phase transition from a ferroelectric tetragonal phase to a paraelectric cubic phase due to heating above 403 K in temperature.

Taking into account the soaring industrial significance of SrF_2, BaF_2 and CaF_2 matrixes, it is only logical that there exist a lot of studies devoted to those materials [36–57]. The SrF_2, BaF_2 and CaF_2 unit cells are equal, and they contain three ions. The cation is located in the coordinate origin (0, 0, 0). The two anions are located at ($\frac{1}{4}$, $\frac{1}{4}$, $\frac{1}{4}$) and ($\frac{3}{4}$, $\frac{3}{4}$, $\frac{3}{4}$). The fluorites SrF_2, BaF_2 and CaF_2 are the cubic $Fm3m$ large-band-gap insulators. Their space group number is 225. The *F*-center in CaF_2 has been observed experimentally by electron-spin-resonance techniques. The *F*-center resonance in CaF_2 has been detected by Arends [58] in additively colored crystals and associated with the optical absorption band at 3.3 eV. Nepomnyashchikh et al. [59] experimentally detected that X-ray irradiation at 77 K of undoped BaF_2 produces V_k and *F*-centers. They have absorption bands at 3.4 and 2.3 eV, respectively [59]. Finally, the experimentally measured *F*-center absorption energy at 4 K temperature in the SrF_2 crystal is equal to 2.85 eV [60]. Present-day knowledge of defects in SrF_2, BaF_2 and CaF_2 crystals has helped to generate the new area of high technology named defect engineering. SrF_2, BaF_2 and CaF_2 crystals could be the important optical materials if we can manage the photo-induced defect process [61,62].

The aim of this contribution is to report our comprehensive ab initio computation results dealing with *F*-centers in $SrZrO_3$, $PbTiO_3$, $BaTiO_3$ and $SrTiO_3$ matrixes, as well as SrF_2, BaF_2 and CaF_2 fluorites. Next, we analyzed our ab initio computation results and created a unified theory, which describes systematic tendencies in ab initio computations dealing with *F*-centers in $SrZrO_3$, $PbTiO_3$, $BaTiO_3$ and $SrTiO_3$ perovskite matrixes, as well as SrF_2, BaF_2 and CaF_2 fluorites.

2. Details of Ab Initio Computations of the *F*-Centers in ABO_3 Perovskites, as Well as in SrF_2, BaF_2 and CaF_2 Fluorites

We computed the *F*-centers in $SrZrO_3$, $PbTiO_3$, $BaTiO_3$ and $SrTiO_3$ perovskites, as well as SrF_2, BaF_2 and CaF_2 fluorites, by means of the CRYSTAL computer program package [63]. For our ab initio *F*-center computations, we used the B3PW hybrid exchange-correlation functional [64]. On the contrary to the plane-wave program packages [65,66], the CRYSTAL brings into play Gaussian-type functions as the basis [63]. It is worth noting that Gaussian-type functions have been intensively investigated during the last years [67,68]. For our numerical computations of *F*-centers in $SrZrO_3$, $PbTiO_3$, $BaTiO_3$ and $SrTiO_3$ perovskites, we

used the basis sets created by Piskunov et al. [69]. We bring into play the $8 \times 8 \times 8$ extension of the Pack Monkhorst mesh [70]. The ABO_3 perovskite *F*-center computations for bulk were performed employing $3 \times 3 \times 3$ extended supercell with 134 atoms and one *F*-center (Figure 1). It is important to note that the generalized-gradient (GGA) and local-density (LDA) approximations to the density functional theory (DFT) strongly underestimate the band gap of insulators and complex oxide materials [46,71]. From another side, the Hartree–Fock (HF) method considerably overestimate the band gap of insulators and complex oxide materials [46,71]. In order to obtain as good as possible results for the band gaps of SrF_2, BaF_2 and CaF_2 fluorites, as well as $SrZrO_3$, $PbTiO_3$, $BaTiO_3$ and $SrTiO_3$ perovskites, we performed our ab initio computations by means of the B3PW hybrid exchange-correlation functional. The B3PW functional contain a portion of exact exchange energy density from the HF method (20%). The rest of the exchange-correlation part consisted of different approaches, including both exchange and correlation. Therefore, the B3PW functional, since it is a superposition of HF and DFT methods, is much better suited for our band gap and optical property (defect level positions in the band gap) ab initio computations in SrF_2, BaF_2, CaF_2, $SrZrO_3$, $PbTiO_3$, $BaTiO_3$ and $SrTiO_3$ matrixes.
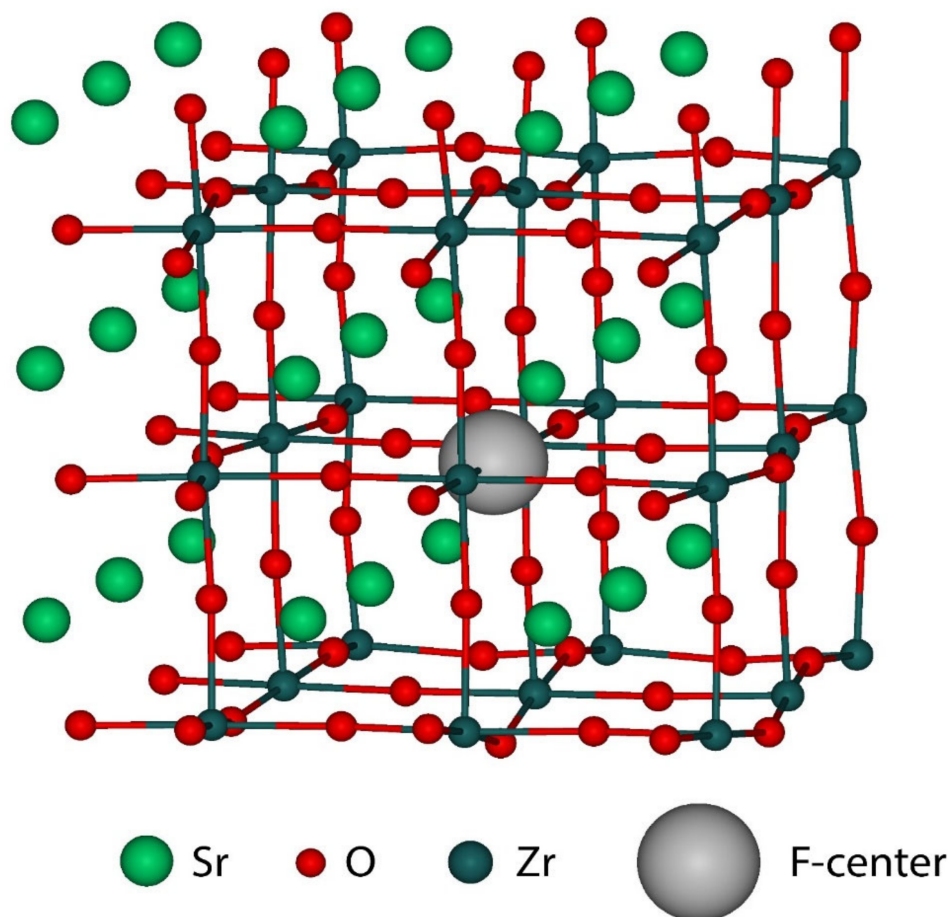

Figure 1. *F*-center in the SrZrO3 bulk, computed by using $3 \times 3 \times 3$ extended supercell.

With aimed to compute the ABO_3 perovskite; for example, for the the $SrZrO_3$ (001) surface *F*-center, we selected a $3 \times 3 \times 1$ times increase in the size of the surface supercells. Namely, with aim to compute the *F*-center situated on the ZrO_2-terminated $SrZrO_3$ (001) surface, we took away the arbitrary surface oxygen atom (Figure 2).
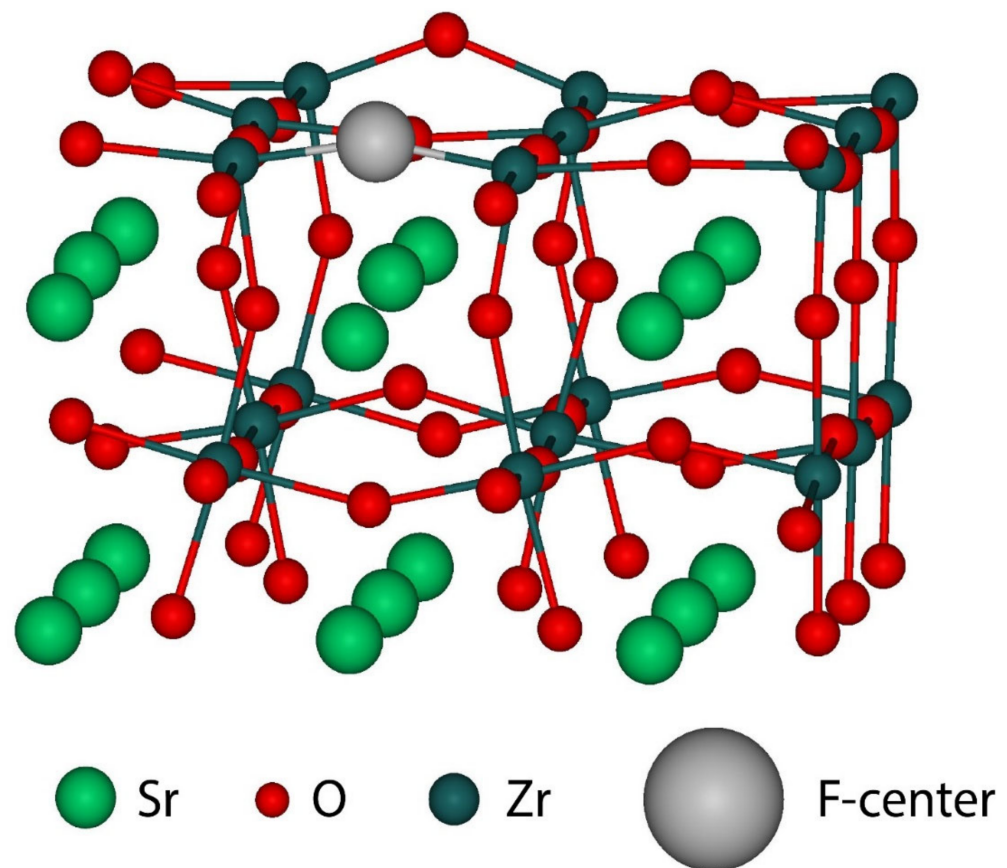
Figure 2. Our ab initio computed *F*-center situated on the $3 \times 3 \times 1$ times increased in size ZrO$_2$-terminated SrZrO$_3$ (001) surface.

In order to maximally exact describe the *F*-center, we used an extra basis function [63]. Namely, we fixed inside the oxygen vacancy auxiliary basis function [63], identical to the commonly named "ghost atom". The formation energy of the bulk oxygen vacancy in ABO$_3$ perovskites was computed by us the using subsequent equation:

$$E^{(F)}{}_{formation} = E(oxygen) + E(F) - E(perfect) \tag{1}$$

where *E*(*oxygen*) is our computed total energy for an oxygen atom, and *E*(*F*) and *E*(*perfect*) are our computed total energies for the *F*-center containing and perfect ABO$_3$ crystal, respectively.

We discuss our computational methodology for *F*-centers in SrF$_2$, BaF$_2$ and CaF$_2$ matrixes by using the CaF$_2$ case as an example. In our *F*-center computations in CaF$_2$ matrix, we used a supercell consisting of 48 atoms (Figure 3). In order to produce the *F*-center, we removed one fluorine atom and kept the supercell charge neutral (Figure 3). To compute the fluorine vacancy with electron (*F*-center) formation energy in CaF$_2$ matrix, we employed the subsequent expression:

$$E^{(F)}{}_{formation} = E(fluorine) + E(F) - E(perfect) \tag{2}$$

where *E*(*fluorine*) is our ab initio computed total energy for the isolated fluorine atom; and *E*(*F*) and *E*(*perfect*) are our ab initio computed total energies for the defective (*F*-center containing) CaF$_2$ crystal and the perfect CaF$_2$ crystal. We utilized the Mulliken representation for the elucidation of the bond populations and the effective atomic charges [72–74].
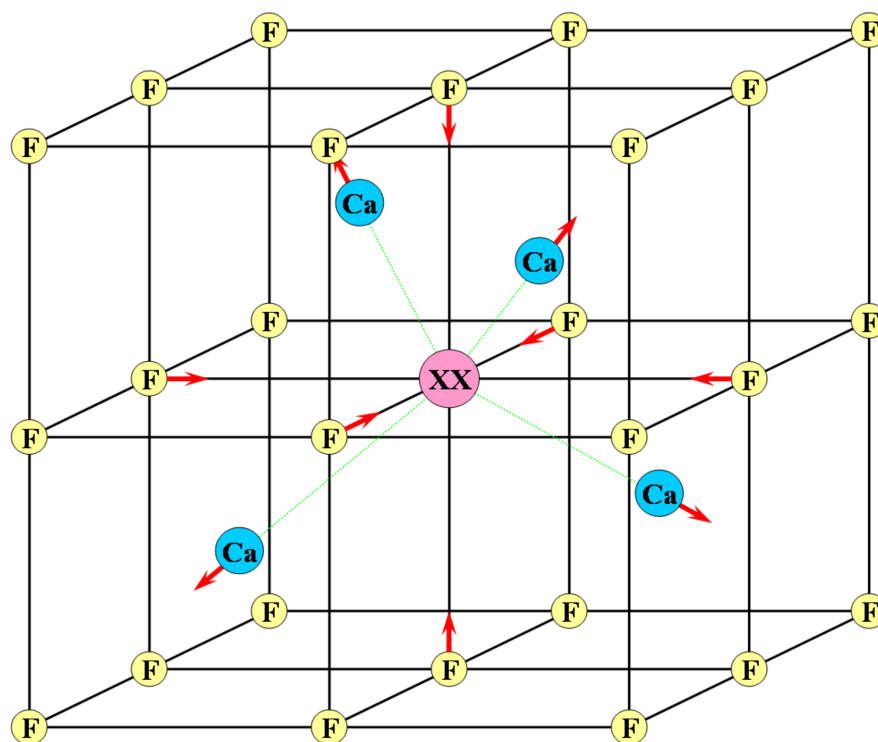
Figure 3. *F*-center (XX) in the CaF$_2$ bulk matrix, computed by using 48-atom supercell.

3. Ab Initio Computation Results for *F*-Centers in ABO$_3$ Perovskites, as Well as in SrF$_2$, BaF$_2$ and CaF$_2$

As an opener of our *F*-center computations in SrZrO$_3$, PbTiO$_3$, BaTiO$_3$, SrTiO$_3$, SrF$_2$, BaF$_2$ and CaF$_2$ matrixes [36,42,75–79], we performed computations for the pristine crystal bulk lattice constants. Our B3PW approximation obtained bulk lattice constants for SrZrO$_3$ (4.163 Å), PbTiO$_3$ (3.936 Å), BaTiO$_3$ (4.008 Å), SrTiO$_3$ (3.904 Å), SrF$_2$ (5.845 Å), BaF$_2$ (6.26 Å) and CaF$_2$ (5.50 Å), and these are in a fair correspondence with the literature's experimental information [80–94] (Table 1). For example, our computed SrTiO$_3$ bulk lattice constant (3.904 Å) is almost in perfect agreement with the experimentally detected SrTiO$_3$ bulk lattice constant (3.89845 Å). Moreover, our ab initio B3PW computed SrF$_2$ (5.845 Å), BaF$_2$ (6.26 Å) and CaF$_2$ (5.50 Å) bulk lattice constants are in a fair agreement with the respective experimental information (5.799, 6.20 and 5.46 Å).

Table 1. Experimental details for pristine SrZrO$_3$, PbTiO$_3$, BaTiO$_3$ and SrTiO$_3$ perovskites, as well as SrF$_2$, BaF$_2$ and CaF$_2$ matrixes [80–94].

Substance	Structure at Room Temperature	Band Gap (eV), Room Temperature	Transition T to Cubic Phase (K)	Experimental Lattice Constant at Cubic Phase (Å)
SrZrO$_3$	Orthorhombic	5.6 [80]	1433 [81]	4.154 [82]
PbTiO$_3$	Tetragonal	3.4 [83]	763 [84]	3.970 [85]
BaTiO$_3$	Tetragonal to orthorhombic	3.38 (// c); 3.27 ($\perp c$) [86]	403 [87]	4.0037 [88]
SrTiO$_3$	Cubic	3.75 [89]	110 [87]	3.89845 [90]
SrF$_2$	Cubic	11.25 [91]	-	5.799 [92]
BaF$_2$	Cubic	11.00 [91]	-	6.20 [93]
CaF$_2$	Cubic	12.1 [91]	-	5.46 [94]

Our computation data, dealing with the atomic shifts around the bulk and (001) surface *F*-centers in SrZrO$_3$, PbTiO$_3$, BaTiO$_3$ and SrTiO$_3$ matrixes, are listed in Table 2.

As we can see from Table 2, all B (Zr or Ti) atoms are repulsed from the bulk and (001) surface *F*-centers in all four our calculated perovskites. The repulsion magnitudes for the Zr atoms from the (001) surface *F*-center located on the ZrO_2-terminated $SrZrO_3$ (001) surface (+9.17% of a_0), as well as for the Ti atoms from the *F*-centers located on the TiO_2-terminated $PbTiO_3$ and $SrTiO_3$ (001) surfaces (+9.98 and +14.0% of a_0), are considerably larger than the B atom repulsion magnitudes from the *F*-centers located in the bulk of $SrZrO_3$, $PbTiO_3$ and $SrTiO_3$ matrixes (+3.68, +1.63 and 7.76% of a_0, respectively). On the contrary, the Ti atom repulsion from the *F*-center located on the BaO-terminated $BaTiO_3$ (001) surface (0.1% of a_0) is smaller than the relevant Ti atom repulsion from the *F*-center located in the $BaTiO_3$ bulk matrix (1.06% of a_0) (Table 2).

Table 2. B3PW computed 3 closest adjacent atom shifts around the bulk and (001) surface *F*-center (in% of the a_0).

| Computed Characteristics	SrZrO₃	PbTiO₃	BaTiO₃	SrTiO₃
Bulk lattice constant (Å)	4.163	3.936	4.008	3.904
Bulk oxygen vacancy in SrZrO₃, PbTiO₃, BaTiO₃ and SrTiO₃ perovskites				
B atom shift (% of a_0)	+3.68	+1.63	+1.06	+7.76
O atom shift (% of a_0)	−2.63	−0.88	−0.71	−7.79
A atom shift (% of a_0)	+0.46	−2.58	−0.08	+3.94
Oxygen vacancy on SrZrO₃, PbTiO₃, BaTiO₃ and SrTiO₃ (001) surface				
B atom shift (% of a_0)	+9.17	+9.98	+0.1	+14.0
O atom shift (% of a_0)	−4.16	−5.58	−1.4	−8.0
A atom shift (% of a_0)	+7.68	-	+1.0	-

The second nearest adjacent O atoms, both in the $SrZrO_3$, $PbTiO_3$, $BaTiO_3$ and $SrTiO_3$ bulk and on its (001) surfaces, always are shifted towards the *F*-center. Namely, the second nearest adjacent O atoms are attracted towards the bulk *F*-center in $SrZrO_3$, $PbTiO_3$, $BaTiO_3$ and $SrTiO_3$ matrixes, by (−2.63, −0.88, −0.71 and −7.79% of a_0, respectively). Even more strongly than in the bulk, the second nearest adjacent O atoms are shifted towards the (001) surface *F*-center in $SrZrO_3$, $PbTiO_3$, $BaTiO_3$ and $SrTiO_3$ perovskites by (−4.16, −5.58, −1.4 and −8.0% of a_0) (Table 2).

According to the ionic model, the net oxygen atom charge is equal to −2 *e*. In our B3PW computations, the oxygen atom charges in pristine $SrZrO_3$, $PbTiO_3$, $BaTiO_3$ and $SrTiO_3$ matrixes are considerably smaller than the classical ionic charges and equal to −1.351 *e*, −1.232 *e*, −1.388 *e* and −1.407 *e* (Table 3). Even less charge is localized inside the bulk oxygen vacancies in $SrZrO_3$, $PbTiO_3$, $BaTiO_3$ and $SrTiO_3$ perovskites, only −1.25 *e*, −0.85 *e*, −1.103 *e* and −1.10 *e*. Our B3PW computed oxygen vacancy formation energies are equal to 7.55, 7.82, 10.30 and 7.10 eV in $SrZrO_3$, $PbTiO_3$, $BaTiO_3$ and $SrTiO_3$ perovskites (Table 3 and Figure 4). Our computed band-gap widths for the $SrZrO_3$, $PbTiO_3$, $BaTiO_3$ and $SrTiO_3$ perovskites, containing the single bulk oxygen vacancy, at the Γ point are equal to 5.07, 2.87, 3.58 and 3.63 eV (Table 3). The oxygen-vacancy-induced defect levels are located inside the band gap, 1.12, 0.96, 0.23 and 0.69 eV below the conduction band (CB) bottom at the Γ-point (Table 3 and Figure 5).

Even less charge is confined in the (001) surface oxygen vacancies in $SrZrO_3$ (−1.10 *e*) and $BaTiO_3$ (−1.052 *e*) matrixes. The (001) surface oxygen vacancy formation energies in $SrZrO_3$, $PbTiO_3$, $BaTiO_3$ and $SrTiO_3$ matrixes are equivalent to 7.52, 5.99, 10.20 and 6.22 eV (Table 3). Finally, the (001) surface-oxygen-vacancy-induced defect level is situated at the Γ-point 0.93, 0.71, 0.07 and 0.25 eV below the CB at $SrZrO_3$, $PbTiO_3$, $BaTiO_3$ and $SrTiO_3$ matrixes (Table 3).

Table 3. B3PW computed electronic structure of the bulk and (001) surface oxygen vacancy in SrZrO$_3$, PbTiO$_3$, BaTiO$_3$ and SrTiO$_3$ matrixes.

Computed Characteristics	SrZrO$_3$	PbTiO$_3$	BaTiO$_3$	SrTiO$_3$
Bulk oxygen vacancy in SrZrO$_3$, PbTiO$_3$, BaTiO$_3$ and SrTiO$_3$ perovskites				
O atom net charge (*e*)	−2.0	−2.0	−2.0	−2.0
O atom charge (*e*) in ABO$_3$	−1.351	−1.232	−1.388	−1.407
F-center charge (*e*)	−1.25	−0.85	−1.103	−1.10
F-cent. format. energy (eV)	7.55	7.82	10.30	7.10
Band gap with *F*-cent. (eV)	5.07	2.87	3.58	3.63
F-center under CB (eV)	1.12	0.96	0.23	0.69
Oxygen vacancy on SrZrO$_3$, PbTiO$_3$, BaTiO$_3$ and SrTiO$_3$ (001) surface				
F-center charge (e)	−1.10	-	−1.052	-
F-cent. format. energy (eV)	7.52	5.99	10.20	6.22
F-center under CB (eV)	0.93	0.71	0.07	0.25
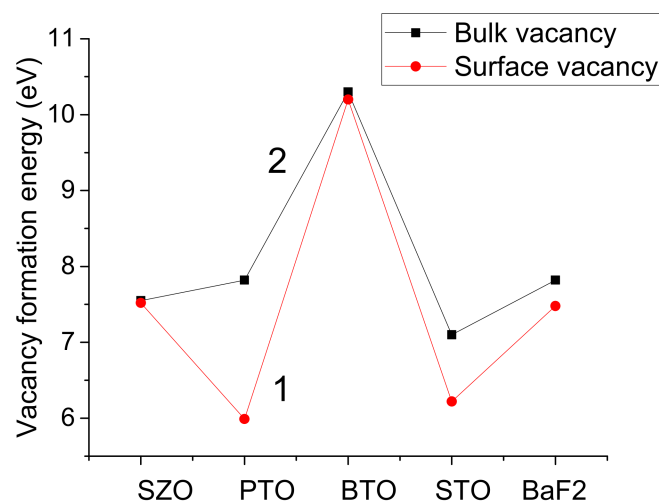
Figure 4. B3PW computed surface (1) and bulk (2) *F*-center formation energies (in eV) in SrZrO$_3$, PbTiO$_3$, BaTiO$_3$, SrTiO$_3$ and BaF$_2$ matrixes.
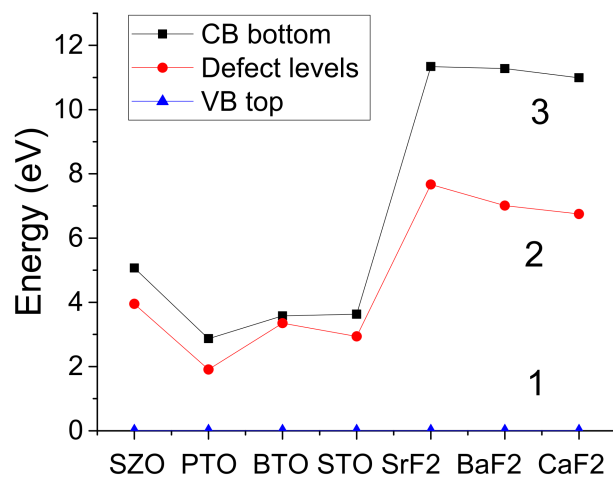
Figure 5. B3PW computed valence band (VB) top (1), conduction band (CB) bottom (3) as well as *F*-center-induced levels (2) between the VB top and CB bottom in the SrZrO$_3$, PbTiO$_3$, BaTiO$_3$, SrTiO$_3$, SrF$_2$, BaF$_2$ and CaF$_2$ bulk matrixes.

In all three pristine SrF_2, BaF_2 and CaF_2 fluorites, our B3PW computed fluorine atom effective charges ($-0.954\ e$, $-0.923\ e$ and $-0.902\ e$) are very close to the net ionic fluorine charge equivalent to $-1.00\ e$ (Table 4). According to our B3PW computations, even less charge is confined inside the bulk fluorine vacancy in the SrF_2, BaF_2 and CaF_2 matrixes ($-0.848\ e$, $-0.801\ e$ and $-0.752\ e$) (Table 4). The nearest Sr atom is sifted towards the bulk fluorine vacancy in the SrF_2 crystal by a very small displacement size (-0.02% of a_0), whereas the nearest Ba and Ca atoms are repulsed from the bulk fluorine vacancy by ($+0.03$ and $+0.15\%$ of a_0) in the BaF_2 and CaF_2 matrixes (Table 4).

Table 4. B3PW computed atomic and electronic structure of the fluorine vacancy in SrF_2, BaF_2 and CaF_2 matrixes.

Computed Bulk Fluorine Vacancy Properties	SrF_2	BaF_2	CaF_2
B3PW computed lattice constant a_0 (Å)	5.845	6.26	5.50
F atom net charge (e)	−1.0	−1.0	−1.0
F atom charge (e) in SrF_2, BaF_2 and CaF_2	−0.954	−0.923	−0.902
Charge inside the fluorine vacancy (e)	−0.848	−0.801	−0.752
A atom shift (% of a_0)	−0.02	+0.03	+0.15
F atom shift (% of a_0)	−0.27	−0.23	+0.28
Fluorine vacancy formation energy (eV)	10.33	7.82	7.87
B3PW calc. band gap, perfect crystal (eV)	11.31	11.30	10.96
B3PW calc. band gap with F-center (eV)	11.34	11.28	10.99
Fluorine vacancy ind. level under CB (eV)	3.67	4.27	4.24
Computed (111) surface fluorine vacancy			
Ba atom shift (% of a_0)	-	−0.13	-
F atom shift (% of a_0)	-	−0.37	-
Charge inside the fluorine vacancy (e)	-	−0.790	-
Fluorine vacancy formation energy (eV)	-	7.48	-
Fluorine vacancy ind. level under CB (eV)	-	4.11	-

The bulk fluorine vacancy formation energy in the SrF_2, BaF_2 and CaF_2 matrixes is equal to 10.33, 7.82 and 7.87 eV, respectively (Table 4 and Figure 4). Our computed band-gap widths for the SrF_2, BaF_2 and CaF_2 containing the single bulk fluorine vacancy at the Γ point are equal to 11.34, 11.28 and 10.99 eV, respectively (Table 4). The bulk-fluorine-vacancy-induced defect levels are located inside the band gap at 3.67, 4.27 and 4.24 eV, respectively, below the conduction band (CB) bottom at the Γ-point in the SrF_2, BaF_2 and CaF_2 matrixes (Table 4 and Figure 5).

Finally, for the fluorine vacancy located on the BaF_2 (111) surface, only the ($-0.790\ e$) charge is localized inside it (Table 4). The nearest Ba atom is shifted towards the (111) surface fluorine vacancy in the BaF_2 matrix by (-0.13% of a_0), and the second nearest F atom is shifted towards the fluorine vacancy even more strongly, by (-0.37% of a_0). The fluorine vacancy formation energy on the BaF_2 (111) surface is equal to 7.48 eV (Table 4). The BaF_2 (111) surface-fluorine-vacancy-induced defect level is located inside the BaF_2 band gap, 4.11 eV below the conduction band (CB) bottom at the Γ-point (Table 4 and Figure 5).

It is worth noting that we observed in our ab initio B3PW computations strong increase of the chemical bond covalency between the F-center and its nearest neighbor cations in our calculated materials. For example, our B3PW computed chemical bond covalency between the Zr and O atoms in the pristine $SrZrO_3$ perovskite is equal to 0.100 e, but the chemical bond covalency between the Zr atoms and bulk F-center in $SrZrO_3$ is more than two times larger and equivalent to 0.244 e. The same situation, according to our B3PW computations, is also in the $BaTiO_3$ perovskite. Namely, the Ti-O chemical bond covalency in the pure $BaTiO_3$ bulk is equivalent to 0.100 e. We observed, according to our ab initio

B3PW computations, the strong increase of the chemical bond covalency between the adjacent Ti atoms and the $BaTiO_3$ bulk F-center equivalent to 0.320 e.

4. Conclusions

The shift magnitudes of the nearest-neighbor atoms around the (001) surface oxygen vacancy in $SrZrO_3$, $PbTiO_3$, $BaTiO_3$ and $SrTiO_3$ perovskites (Table 3), in most cases, are larger than the respective shift magnitudes of the nearest atoms around the bulk oxygen vacancy. The atomic shift amplitudes around both (001) surface and bulk oxygen vacancies in $SrZrO_3$, $PbTiO_3$, $BaTiO_3$ and $SrTiO_3$ perovskites (Table 3) almost always are significantly larger than the atomic shift magnitudes around the fluorine vacancy in SrF_2, BaF_2 and CaF_2 fluorites (Table 4).

In the $SrZrO_3$, $PbTiO_3$, $BaTiO_3$ and $SrTiO_3$ perovskites, the charge, as a rule, is much better localized inside the bulk oxygen vacancy than inside the (001) surface oxygen vacancy (Table 3). In ionic materials, such as, SrF_2, BaF_2 and CaF_2, the charge is considerably better localized (Table 4) inside the fluorine vacancy than inside the oxygen vacancy of $SrZrO_3$, $PbTiO_3$, $BaTiO_3$ and $SrTiO_3$ perovskites (Table 3). More than 75% of charge is localized inside the bulk and (111) surface fluorine vacancy in the SrF_2, BaF_2 and CaF_2 matrixes (Table 4). We obtained the strong increase of a chemical bond covalency among the F-center and its nearest adjoining cations, in comparison to the pristine crystals.

In the $SrZrO_3$, $PbTiO_3$, $BaTiO_3$ and $SrTiO_3$ perovskites, as well as BaF_2 fluorite, the surface-oxygen-induce or fluorine-vacancy-induced defect levels are located closer to the CB band bottom than in the bulk cases (Tables 3 and 4). The B3PW computed energy difference between the $SrZrO_3$, $PbTiO_3$, $BaTiO_3$, $SrTiO_3$ and CaF_2 bulk and surface oxygen or fluorine vacancies (Tables 3 and 4) triggers the vacancy segregation from the bulk towards the surface.

Our computation results for the F-center defect ground state levels in CaF_2, BaF_2 and SrF_2 fluorites, located at 4.24, 4.27 and 3.67 eV under the CB bottom, suggest a possible explanation of the optical absorption observed experimentally in CaF_2, BaF_2 and SrF_2 fluorites at 3.3, 2.3 and 2.85 eV. According to our computations, the experimentally observed optical absorption may be due to an electron transition from the F-center ground state, located at 4.24, 4.27 and 3.67 eV under the CB, to the CB. Namely, rhe F-center defect band at CaF_2, BaF_2 and SrF_2 is located 4.24, 4.27 and 3.67 eV under the CB, which is very close to the experimentally detected optical absorption energy equal to 3.3, 2.3 and 2.85 eV, respectively.

Institutional Review Board Statement: Not applicable.

Informed Consent Statement: Not applicable.

Data Availability Statement: Not applicable.

Conflicts of Interest: The authors declare no conflict of interests.

References

1. Kotomin, E.A.; Popov, A.I. Radiation-induced point defects in simple oxides. *Nucl. Instrum. Methods Phys. Res. Sect. B* **1998**, *141*, 1–15. [CrossRef]
2. Popov, A.I.; Kotomin, E.A.; Maier, J. Basic properties of the *F*-type centers in halides, oxides and perovskites. *Nucl. Instrum. Methods Phys. Res. Sect. B* **2010**, *268*, 3084–3089. [CrossRef]
3. Itoh, N. Creation of lattice defects by electronic excitation in alkali halides. *Adv. Phys.* **1982**, *31*, 491–551. [CrossRef]
4. Itoh, N.; Tanimura, K. Formation of interstitial-vacancy pairs by electronic excitation in pure ionic-crystals. *J. Phys. Chem. Solids* **1990**, *51*, 717–735. [CrossRef]
5. Lushchik, C.; Lushchik, A. Evolution of Anion and Cation Excitons in Alkali Halide Crystals. *Phys. Solid State* **2018**, *60*, 1487–1505. [CrossRef]
6. Dauletbekova, A.; Akilbekov, A.; Elango, A. Thermo-and Photostimulated Recombinations of F-H_A and α-I_A Centres in KBr with Large Na Concentration. *Phys. Stat. Sol. B* **1982**, *112*, 445–452. [CrossRef]
7. Kirm, M.; Lushchik, A.; Lushchik, C.; Martinson, I.; Nagirnyi, V.; Vasil'chenko, E. Creation of groups of spatially correlated defects in a KBr crystal at 8 K. *J. Phys. Condens. Matter* **1998**, *10*, 3509–3521. [CrossRef]
8. Weinstein, I.A.; Kortov, V.S.; Vohmintsev, A.S. The compensation effect during luminescence of anion centers in aluminum oxide. *J. Lumin.* **2007**, *122*, 342–344. [CrossRef]
9. Feldbach, E.; Toldsepp, E.; Kirm, M.; Lushchik, A.; Mizohata, K.; Raisanen, J. Radiation resistance diagnostics of wide-gap optical materials. *Opt. Mater.* **2016**, *55*, 164–167. [CrossRef]
10. Ananchenko, D.V.; Nikiforov, S.V.; Konev, S.F.; Ramazanova, G.R. ESR and luminescent properties of anion-deficient α-Al_2O_3 single crystals after high-dose irradiation by a pulsed electron beam. *Opt. Mater.* **2019**, *90*, 118–122. [CrossRef]
11. Lushchik, A.; Karner, T.; Lushchik, C.; Vasilchenko, E.; Dolgov, S.; Issahanyan, V.; Liblik, P. Dependence of long-lived defect creation on exciton density in MgO single crystals. *Phys. Stat. Sol. C* **2007**, *4*, 1084–1087.
12. Myasnikova, L.; Shunkeyev, K.; Zhanturina, N.; Ubaev, Z.; Barmina, A.; Sagimbaeva, S.; Aimaganbetova, Z. Luminescence of self-trapped excitons in alkali halide crystals at low temperature uniaxial deformation. *Nucl. Instrum. Methods Phys. Res. Sect. B* **2020**, *464*, 95–99. [CrossRef]
13. Schweizer, S.; Secu, M.; Spaeth, J.M.; Hobs, L.W.; Edgar, A.; Williams, G.V.M. New developments in X-ray storage phosphors. *Radiat. Meas.* **2004**, *38*, 633–638. [CrossRef]
14. Elango, A.; Sagimbaeva, S.; Sarmukhanov, E.; Savikhina, T.; Shunkeev, K. Effect of uniaxial stree on luminescence of X- and VUV-irradiated NaCl and NaBr crystals. *Radiat. Meas.* **2001**, *33*, 823–827. [CrossRef]
15. Kortov, V.; Lushchik, A.; Nagirnyi, V.; Ananchenko, D.; Romet, I. Spectrally resolved thermally stimulated luminescence of irradiated anion-defective alumina single crystals. *J. Lumin.* **2017**, *186*, 189–193. [CrossRef]
16. Koyama, T.; Suemoto, T. Dynamics of nuclear wave packets at the *F* center in alkali halides. *Rep. Prog. Phys.* **2011**, *74*, 076502. [CrossRef]
17. Skuratov, V.A.; O'Connell, J.; Kirilkin, N.S.; Neethling, J. On the threshold of damage formation in aluminium oxide via electronic excitations. *Nucl. Instrum. Methods Phys. Res. Sect. B* **2014**, *326*, 223–227. [CrossRef]
18. Van Vuuren, J.A.; Saifulin, M.M.; Skuratov, V.A.; O'Connell, J.H.; Aralbayeva, G.; Dauletbekova, A.; Zdorovets, M. The influence of stopping power and temperature on latent track formation in YAP and YAG. *Nucl. Instrum. Methods Phys. Res. Sect. B* **2019**, *460*, 67–73. [CrossRef]
19. Mota, F.; Ortiz, C.J.; Vila, R.; Casal, N.; Garcia, A.; Ibarra, A. Calculation of damage function of Al_2O_3 in irradiation facilities for fusion reactor applications. *J. Nucl. Mater.* **2013**, *442*, S699–S704. [CrossRef]
20. Dukenbayev, K.; Kozlovskiy, A.; Kenzhina, I.; Berguzinov, A.; Zdorovets, M. Study of the effect of irradiation with Fe^{7+} ions on the structural properties of thin TiO_2 foils. *Mater. Res. Express* **2019**, *6*, 046309. [CrossRef]
21. Zdorovets, M.; Dukenbayev, K.; Kozlovskiy, A.; Kenzhina, I. Defect formation in AlN after irradiation with He^{2+} ions. *Ceram. Int.* **2019**, *45*, 8130–8137. [CrossRef]
22. Janesco, B.G.; Jones, S.I. Quantifying the delocalization of surface and bulk *F*-centers. *Surf. Sci.* **2017**, *659*, 9–15. [CrossRef]
23. Eglitis, R.I.; Christensen, N.E.; Kotomin, E.A.; Postnikov, A.V.; Borstel, G. First-principles and semiempirical calculations for *F* center in $KNbO_3$. *Phys. Rev. B* **1997**, *56*, 8599–8604. [CrossRef]
24. Carballo-Cordova, D.A.; Ochoa-Lara, M.T.; Olive-Mendez, S.F.; Espinosa-Magana, F. First-principles calculations and Bader analysis of oxygen-deficient induced magnetism in cubic $BaTiO_{3-x}$ and $SrTiO_{3-x}$. *Philos. Mag.* **2019**, *99*, 181–187. [CrossRef]
25. Ojha, S.K.; Gogoi, S.K.; Mandal, P.; Kaushik, S.D.; Freeland, J.W.; Jain, M.; Middey, S. Oxygen vacancy induced electronic structure modification of $KTaO_3$. *Phys. Rev. B* **2021**, *103*, 085102. [CrossRef]
26. Osinkin, D.A.; Khodimchuk, A.V.; Porotnikova, N.M.; Bogdanovich, N.M.; Fetisov, A.V.; Ananyev, M.V. Rate-Determining Steps of Oxygen Surface Exchange Kinetics on $Sr_2Fe_{1.5}Mo_{0.5}O_{6-\delta}$. *Energies* **2020**, *13*, 250. [CrossRef]
27. Farlenkov, A.S.; Ananyev, M.V.; Eremin, V.A.; Porotnikova, N.M.; Kurumchin, E.K.; Melehov, B.T. Oxygen isotope exchange in doped calcium and barium zirconates. *Solid State Ion.* **2016**, *290*, 108–115. [CrossRef]
28. Mueller, D.N.; Machala, M.L.; Bluhm, H.; Chueh, W.C. Redox activity of surface oxygen anions in oxygen-deficient perovskite oxides during electrochemical reactions. *Nat. Commun.* **2015**, *6*, 6097. [CrossRef]

29. Ji, Q.; Bi, L.; Zhang, J.; Cao, H.; Zhao, X.S. The role of oxygen vacancies of ABO_3 perovskite oxides in the oxygen reduction reaction. *Energy Environ. Sci.* **2020**, *13*, 1408–1428. [CrossRef]

30. Su, H.Y.; Sun, K. DFT study of the stability of oxygen vacancy in cubic ABO_3 perovskites. *J. Mater. Sci.* **2015**, *50*, 1701–1709. [CrossRef]

31. Eglitis, R.I. Ab initio calculations of $SrTiO_3$, $BaTiO_3$, $PbTiO_3$, $CaTiO_3$, $SrZrO_3$, $PbZrO_3$ and $BaZrO_3$ (001), (011) and (111) surfaces as well as *F* centers, polarons, KTN solid solutions and Nb impurities therein. *Int. J. Mod. Phys. B* **2014**, *28*, 1430009. [CrossRef]

32. Crespillo, M.L.; Graham, J.T.; Agullo-Lopez, F.; Zhang, Y.W.; Weber, W.J. Real-Time Identification of Oxygen Vacancy Centers in $LiNbO_3$ and $SrTiO_3$ during Irradiation with High Energy Particles. *Crystals* **2021**, *11*, 315. [CrossRef]

33. Jiao, X.P.; Liu, T.Y.; Lu, Y.Z.; Li, Q.Y.; Guo, R.; Wang, X.L.; Xu, X. Optical Properties of the Oxygen Vacancy in $KNbO_3$ Crystal. *J. Electron. Mater.* **2020**, *49*, 2137–2143. [CrossRef]

34. Eglitis, R.I.; Popov, A.I.; Purans, J.; Jia, R. First principles hybrid Hartree-Fock-DFT calculations of bulk and (001) surface *F* centers in oxide perovskites and alkali-earth fluorides. *Low Temp. Phys.* **2020**, *46*, 1206–1212. [CrossRef]

35. Gu, X.K.; Samira, S.; Nikolla, E. Oxygen Sponges for Electrocatalysis: Oxygen Reduction/Evolution on Nonstoichiometric, Mixed Metal Oxides. *Chem. Mater.* **2018**, *30*, 2860–2872. [CrossRef]

36. Shi, H.; Eglitis, R.I.; Borstel, G. Ab initio calculations of the CaF_2 electronic structure and *F* centers. *Phys. Rev. B* **2005**, *72*, 045109. [CrossRef]

37. Wen, C.; Lanza, M. Calcium fluoride as high-k dielectric for 2D electronics. *Appl. Phys. Reviews* **2021**, *8*, 021307.

38. Laanaiya, M.; Bouibes, A.; Zaoui, A. Ground state properties of fluorine from DFT-hybrid functional. *Vacuum* **2021**, *187*, 110118. [CrossRef]

39. Weng, J.P.; Gao, S.P. Layer-dependent band gaps and dielectric constants of ultrathin fluorite crystals. *J. Phys. Chem. Solids* **2021**, *148*, 109738. [CrossRef]

40. Liebig, A.; Hapala, P.; Weymouth, A.J.; Giessibl, F.J. Quantifying the evolution of atomic interaction of a complex surface with a functionalized atomic force microscopy tip. *Sci. Rep.* **2020**, *10*, 14104. [CrossRef]

41. Ryabochkina, P.A.; Krushchalina, S.A.; Yurlov, I.A.; Egorysheva, A.V.; Atanova, A.V.; Veselova, V.O.; Kyashkin, V.M. Blackbody emission from CaF_2 and ZrO_2 nanosized electric particles doped with Er^{3+} ions. *RSC Adv.* **2020**, *10*, 26288–26297. [CrossRef]

42. Shi, H.; Eglitis, R.I.; Borstel, G. Ab initio calculations of the BaF_2 bulk and surface *F* centres. *J. Phys. Condens. Matter* **2006**, *18*, 8367–8381. [CrossRef]

43. Cappellini, G.; Bosin, A.; Serra, G.; Furthmüller, J.; Bechstedt, F.; Botti, S. Electronic and Optical Properties of Small Metal Fluoride Clusters. *ACS Omega* **2020**, *5*, 13268–13277. [CrossRef] [PubMed]

44. Pawlik, N.; Szpikowska-Sroka, B.; Goryczka, T.; Pisarski, W.A. Spectroscopic Properties of Eu^{3+} Ions in Sol-Gel Materials Containing Calcium Fluoride Nanocrystals. *Phys. Stat. Sol. B* **2020**, *257*, 1900478. [CrossRef]

45. Matusalem, F.; Marques, M.; Teles, L.K.; Filippetti, A.; Cappellini, G. Electronic properties of fluorides by efficient approximated quasiparticle DFT-1/2 and PSIC methods. *J. Phys. Condens. Matter* **2018**, *30*, 365501. [CrossRef] [PubMed]

46. Vassilyeva, A.F.; Eglitis, R.I.; Kotomin, E.A.; Dauletbekova, A.K. Ab initio calculations of MgF_2 (001) and (011) surface structure. *Physica B* **2010**, *405*, 2125–2127. [CrossRef]

47. Shi, H.; Chang, L.; Jia, R.; Eglitis, R.I. Ab initio calculations of the charge transfer and aggregation of *F* centers in CaF_2. *J. Phys. Chem. C* **2012**, *116*, 4832–4839. [CrossRef]

48. Häfner, M.; Bredow, T. Mobility of *F* Centers in Alkali Halides. *J. Phys. Chem. C* **2021**, *125*, 9085–9095. [CrossRef]

49. Mir, A.; Zaoui, A.; Bensaid, D. The displacement effect of a fluorine atom in CaF_2 on the band structure. *Appl. Surf. Sci.* **2018**, *439*, 1180–1185. [CrossRef]

50. Ibraheem, A.M.; Khalafalla, M.A.H.; Eisa, M.H. First principle calculation of accurate native defect levels in CaF_2. *Eur. Phys. J. B* **2017**, *90*, 42. [CrossRef]

51. Shi, H.; Jia, R.; Eglitis, R.I. First-principles calculations of surface H centers in BaF_2. *Phys. Rev. B* **2010**, *81*, 195101. [CrossRef]

52. Andrade, A.B.; Ferreira, N.S.; Valerio, M.E.G. Particle size effects on structural and optical properties of BaF_2 nanoparticles. *RSC Adv.* **2017**, *7*, 26839–26848. [CrossRef]

53. Watanabe, M.; Azuma, J.; Asaka, S.; Tsujibayashi, T.; Arimoto, O.; Nakanishi, S.; Itoh, H.; Kamada, M. Photostimulated detection of defect formation in BaF_2 under irradiation of synchrotron radiation. *Phys. Stat. Sol. B* **2013**, *250*, 396–401. [CrossRef]

54. Shi, H.; Jia, R.; Eglitis, R.I. First-principles simulations on the aggregation of *F* centers in BaF_2: *R* centers. *Solid State Ion.* **2011**, *187*, 1–7. [CrossRef]

55. Hoya, J.; Laborde, J.I.; Richard, D.; Renteria, M. Ab initio study of *F*-centers in alkali halides. *Comput. Mater. Sci.* **2017**, *139*, 1–7.

56. Shi, H.; Chang, L.; Jia, R.; Eglitis, R.I. Ab initio calculations of hydroxyl impurities in CaF_2. *J. Phys. Chem. C* **2012**, *116*, 6392–6400. [CrossRef]

57. Cen, J.; Liang, F.; Chen, D.L.; Zhang, L.L.; Yang, N.; Zhu, W.D. Adsorption of water molecule on calcium fluoride and magnesium fluoride surfaces: A combined Theoretical and experimental study. *J. Phys. Chem. C* **2020**, *124*, 7853–7859. [CrossRef]

58. Arends, J. Color centers in additively colored CaF_2 and BaF_2. *Phys. Stat. Sol. B* **1964**, *7*, 805–815. [CrossRef]

59. Nepomnyashchikh, A.I.; Radzhabov, E.A.; Egranov, A.V.; Ivashechkin, V.F.; Istomin, A.S. Defect formation and VUV luminescence in BaF_2. *Radiat. Eff. Defects Solids* **2002**, *157*, 715–719. [CrossRef]

60. Cavenett, B.C.; Hayes, W.; Hunter, I.C.; Stoneham, A.M. Magneto optical properties of *F* centres in alkaline earth fluorides. *Proc. R. Soc. Lond. Ser. A* **1969**, *309*, 53–68.

61. Assylbayev, R.; Lushchik, A.; Lushchik, C.; Kudryavtseva, I.; Shablonin, E.; Vasilchenko, E.; Akilbekov, A.; Zdorovets, M. Structural defects caused by swift ions in fluorite single crystals. *Opt. Mater.* **2018**, *75*, 196–203. [CrossRef]

62. Batool, A.; Izerrouken, M.; Aisida, S.O.; Hussain, J.; Ahmad, I.; Afzal, M.Q. Effect of Ca colloids on in-situ ionoluminescence of CaF_2 sigle crystals. *Nucl. Instrum. Methods Phys. Res. Sect. B* **2020**, *476*, 40–43. [CrossRef]

63. Saunders, V.R.; Dovesi, R.; Roetti, C.; Causa, N.; Harrison, N.M.; Orlando, R.; Zicovich-Wilson, C.M. *Crystal-2009 User Manual*; University of Torino: Torino, Italy, 2009.

64. Perdew, J.P.; Wang, Y. Accurate and simple analytic representation of the electron-gas correlation energy. *Phys. Rev. B* **1992**, *45*, 13244–13249. [CrossRef] [PubMed]

65. Cohen, R.E. Surface effects in ferroelectrics: Periodic slab computations for $BaTiO_3$. *Ferroelectrics* **1997**, *194*, 323–342. [CrossRef]

66. Cohen, R.E. Periodic slab LAPW computations for ferroelectric $BaTiO_3$. *J. Phys. Chem. Solids* **1996**, *57*, 1393–1396. [CrossRef]

67. Shang, Y. Lower bounds for Gaussian Estrada index of graphs. *Symmetry* **2018**, *10*, 325. [CrossRef]

68. Alhevaz, A.; Baghipur, M.; Shang, Y. On generalized distance Gaussian Estrada index of graps. *Symmetry* **2019**, *11*, 1276. [CrossRef]

69. Piskunov, S.; Heifets, E.; Eglitis, R.I.; Borstel, G. Bulk properties and electronic structure of $SrTiO_3$, $BaTiO_3$, $PbTiO_3$ perovskites: An ab initio HF/DFT study. *Comput. Mater. Sci.* **2004**, *29*, 165–178. [CrossRef]

70. Monkhorst, H.J. Special points for Brillouin-zone integrations. *Phys. Rev. B* **1976**, *13*, 5188. [CrossRef]

71. Eglitis, R.I. Ab initio calculations of the atomic and electronic structure of $BaZrO_3$ (111) surfaces. *Solid State Ion.* **2013**, *230*, 43–47. [CrossRef]

72. Mesquita, W.D.; Oliveira, M.C.; Assis, M.; Ribeiro, R.A.P.; Eduardo, A.C.; Teordoro, M.D.; Marques, G.E.; Júnior, M.G.; Longo, E.; Gurgel, M.F.C. Unraveling the relationship between bulk structure and exposed surfaces and its effect on the electronic structure and photoluminescent properties of $Ba_{0.5}Sr_{0.5}TiO_3$: A joint experimental and theoretical approach. *Mater. Res. Bull.* **2021**, *143*, 111442. [CrossRef]

73. Eglitis, R.I.; Kleperis, J.; Purans, J.; Popov, A.I.; Jia, R. Ab initio calculations of $CaZrO_3$ (011) surfaces: Systematic trends in polar (011) surface calculations of ABO_3 perovskites. *J. Mater. Sci.* **2020**, *55*, 203–217. [CrossRef]

74. Eglitis, R.I.; Purans, J.; Gabrusenoks, J.; Popov, A.I.; Jia, R. Comparative ab initio calculations of ReO_3, $SrZrO_3$, $BaZrO_3$, $PbZrO_3$ and $CaZrO_3$ (001) surfaces. *Crystals* **2020**, *10*, 745. [CrossRef]

75. Eglitis, R.I.; Piskunov, S. First principles calculations of $SrZrO_3$ bulk and ZrO_2-terminated (001) surface F centers. *Comput. Condens. Matter* **2016**, *7*, 1–6. [CrossRef]

76. Zhukovskii, Y.F.; Kotomin, E.A.; Piskunov, S.; Ellis, D.E. A comparative ab initio study of bulk and surface oxygen vacancies in $PbTiO_3$, $PbZrO_3$ and $SrTiO_3$ perovskites. *Solid State Commun.* **2009**, *149*, 1359–1362. [CrossRef]

77. Sokolov, M.; Eglitis, R.I.; Piskunov, S.; Zhukovskii, Y.F. Ab initio hybrid DFT calculations of $BaTiO_3$ bulk and BaO-terminated (001) surface F-centers. *Int. J. Mod. Phys. B* **2017**, *31*, 1750251. [CrossRef]

78. Carrasco, J.; Illas, F.; Lopez, N.; Kotomin, E.A.; Zhukovskii, Y.F.; Evarestov, R.A.; Mastrikov, Y.A.; Piskunov, S.; Maier, J. First-principles calculations of the atomic and electronic structure of F centers in the bulk and on the the (001) surface of $SrTiO_3$. *Phys. Rev. B* **2006**, *73*, 064106. [CrossRef]

79. Jia, R.; Shi, H.; Borstel, G. Ab initio calculations for SrF_2 with F and M centers. *Comput. Mater. Sci.* **2008**, *43*, 980–988. [CrossRef]

80. Lee, Y.S.; Lee, J.S.; Noh, T.W.; Byun, D.Y.; Yoo, K.S.; Yamaura, K.; Takayama-Muromachi, E. Systematic trends in the electronic structure parameters of the $4d$ transition-metal oxides $SrMO_3$ (M = Zr, Ru and Rh). *Phys. Rev. B* **2003**, *67*, 113101. [CrossRef]

81. Yoshino, M.; Yukawa, H.; Morinaga, M. Modification of local electronic structures due to phase transition in perovskite-type oxides, $SrBO_3$ (B = Zr, Ru, Hf). *Mater. Trans.* **2004**, *45*, 2056–2061. [CrossRef]

82. Kennedy, B.J.; Howard, C.J.; Chakoumakos, B.C. High-temperature phase transitions in $SrZrO_3$. *Phys. Rev. B* **1999**, *59*, 4023–4027. [CrossRef]

83. Robertson, J. Band offsets of wide-band-gap oxides and implications for future electronic devices. *J. Vacuum Sci. Technol.* **2000**, *18*, 1785–1791. [CrossRef]

84. Nelmes, R.J.; Kuhs, W.F. The crystal structure of tetragonal $PbTiO_3$ at room temperature and at 700 K. *Solid State Commun.* **1985**, *54*, 721–723. [CrossRef]

85. Mabud, S.A.; Glazer, A.M. Lattice parameters and birefringence in $PbTiO_3$ single crystals. *J. Appl. Cryst.* **1979**, *12*, 49–53. [CrossRef]

86. Wemple, S.H. Polarization fluctuations and the optical-absorption edge in $BaTiO_3$. *Phys. Rev. B* **1970**, *2*, 2679–2689. [CrossRef]

87. Meyer, B.; Padilla, J.; Vanderbilt, D. Theory of $PbTiO_3$, $BaTiO_3$ and $SrTiO_3$ surfaces. *Faraday Discuss.* **1999**, *114*, 395–405. [CrossRef]

88. Edwards, J.W.; Speiser, R.; Johnston, H.L. Structure of barium titanate at elevated temperatures. *J. Amer. Chem. Soc.* **1951**, *73*, 2934–2935. [CrossRef]

89. van Benthem, K.; Elsasser, C.; French, R.H. Bulk electronic structure of $SrTiO_3$: Experiment and theory. *J. Appl. Phys.* **2001**, *90*, 6156–6164. [CrossRef]

90. Sato, M.; Soejima, Y.; Ohama, N.; Okazaki, A.; Scheel, H.J.; Müller, K.A. The lattice constant vs temperature relation around the 105 K transition of a flux-grown $SrTiO_3$ crystal. *Phase Trans.* **1985**, *5*, 207–218. [CrossRef]

91. Rubloff, G.W. Far-Ultraviolet Reflectence Spectra and the Electronic Structure of Ionic Crystals. *Phys. Rev. B* **1972**, *5*, 662–684. [CrossRef]

92. Hayes, W. *Crystals with the Fluorite Structure*; Clarendon Press: Oxford, UK, 1974.
93. Leger, J.M.; Haines, J.; Atouf, A.; Schulte, O. High-pressure x-ray and neutron-diffraction studies of BaF_2: An example of a coordination number of 11 in AX_2 compounds. *Phys. Rev. B* **1995**, *52*, 13247. [CrossRef] [PubMed]
94. Nicolav, M. Shaped single crystals of CaF_2. *J. Cryst. Growth* **2000**, *218*, 62–66. [CrossRef]